

Spectating the proton migration on catalyst with noninnocent ligand in aqueous electrochemical CO₂ reduction

Yangfan Li ^{a,b,1}, Shijie Xie ^{a,b,1}, Xingmiao Huang ^{a,b}, Wenjing Song ^{a,b}, Chuncheng Chen ^{a,b}, Hua Sheng ^{a,b,*}, Jincai Zhao ^{a,b}

^a Key Laboratory of Photochemistry, Institute of Chemistry, Chinese Academy of Sciences, Beijing National Laboratory for Molecular Sciences, Beijing 100190, PR China

^b University of Chinese Academy of Sciences, Beijing 100049, PR China



ARTICLE INFO

Keywords:
Proton transfer
IR spectroscopy
CO₂ reduction
Noninnocent ligand
Molecular complex

ABSTRACT

It is of great significance to investigate aqueous CO₂ reduction on catalysts with redox-noninnocent ligands as they effectively facilitate CO₂ reduction but circumvent the H₂ evolution. By developing the methodology of rapid-scan FT-IR in external reflection mode, the pathway of CO₂ reduction on iron porphyrin was in-situ monitored. It's uncovered that coupled with first-electron reduction of [Fe^{II}TAPP]⁰, the porphyrin nitrogen is protonated as the observation of NH⁺ ammonium band in IR spectra, which avoids the formation of Fe-H structure for proton reduction. Moreover, an inverse kinetic isotope effect (KIE = 0.59) in formation of *COOH indicates the protonated porphyrin-N would also act as a proton relay for the efficient inner-sphere proton transfer to the activated CO₂ molecules. This work experimentally identified the proton migration pathway via the reduced porphyrin ligand as proton shuttle for the first time and should benefit the design of the catalyst of high CO₂ reduction selectivity.

1. Introduction

Owing to the continuously increased atmospheric CO₂ levels, the electrochemical reduction of CO₂ has raised significant current interests for its potential application in converting the greenhouse gas CO₂ to fuels or industrial feed stocks with the utilization of clean energy [1]. In an electrochemical system, the selection of solvent/electrolyte is decisive when considering its critical effects in both the reaction efficiency and product distribution, but the proceeding of CO₂ reduction in aqueous media is significantly preferred beyond such consideration, not only due to the obvious benefit by employing a universal and environmentally friendly solvent/electrolyte but also the easy association with the water oxidation reaction, the half reaction in the natural photosynthesis, to establish a closed artificial photosynthesis system [2]. However, to achieve efficient and highly selective CO₂ reduction in aqueous system is of a great challenge: the poor solubility of CO₂ (0.0383 M) in protic solvent of water situates it at an obvious disadvantage when competing with proton reduction [3].

For another aspect, in spite of being competing reactions, the most

intriguing aspect in the relevance between CO₂ reduction and proton reduction is that the protons also positively participate in the CO₂ reduction, e.g., the protonation of the one-electron reduced intermediate of *CO₂^{*} to form *COOH is critical for the following breakage of C-O bond to form CO, and for the further reduced hydrocarbons like methane, the proton transfer is also demanded for the formation of C-H bond in the intermediate of *CHO [4,5]. Moreover, owing to the nature of CO₂ reduction being a complex procedure involving both electron and proton transfer, a proton-coupled electron transfer (PCET) process is always more desired than the stepwise electron/proton transfer, which significantly reduces the over-potential by avoiding the formation of charged intermediates with high activation barrier [6,7]. Therefore, a delicate transfer of the protons to favor the CO₂ reduction while avoiding the reduction of themselves should be pivotal for the highly selective CO₂ reduction.

In this regard, various homogeneous and heterogeneous catalysts have been explored to meet this requirements, but in aqueous media, only a very small fraction of them were reported to exhibit the high selectivity towards the CO₂ reduction rather than the proton reduction

* Corresponding author at: Key Laboratory of Photochemistry, Institute of Chemistry, Chinese Academy of Sciences, Beijing National Laboratory for Molecular Sciences, Beijing 100190, PR China.

E-mail address: hsheng@iccas.ac.cn (H. Sheng).

¹ Authors made equal contributions

to H₂. Importantly, transition metal complexes involving noninnocent ligands including porphyrins, phthalocyanine, bipyridines is just a group of most popular catalysts are able to maintain high selectivity of CO₂ reduction reaction (CO₂RR) even in aqueous solution [8–10]. Thus, understanding the behavior of noninnocent ligands in electrochemical reaction is very important for design more efficient catalysts. Although different spectroscopic technology such as Mössbauer, [11] electron paramagnetic resonance (EPR) [12] and X-ray absorption (XAS) [13] have been used to probe state of metal center, the cognition of ligand noninnocence still mostly focus on helping electron storage or delocalization to promote multielectron-transfer process [14]. Recently theoretical calculation claim that reduced ligand may lead to form ligand-hydride instead of metal-hydride, while it's of great challenge to trace proton migration in aqueous CO₂ reduction that involved complicated multi-electron/proton transfer [15,16]. Nevertheless, more advanced electrochemical spectroscopy is needed to provide direct evidence of proton transfer in aqueous electrochemical CO₂ reduction.

Herein, based on the rapid-scan FT-IR method we reported previously, [17–20] we further developed an external reflection infrared spectroscopy methodology for the in-situ monitoring of the aqueous electrochemical CO₂ reduction in molecular catalytic system. The model catalyst employed here is iron porphyrin with four positively charged N, N,N-trimethyl-4-ammonium-phenyl substituents (abbreviated as FeTAPP, the structure of which was shown in Fig. 2b) discovered by Robert et al., [21,22] which is one of most explored water-soluble molecular catalysts with noninnocent ligand for CO₂ reduction. That is noted that a water-soluble catalyst is free of immobilization on carbon materials which helps eliminate effect of substrate. By synchronizing the infrared spectrometer with linear sweep voltammetry or chronoamperometry scan, a series of potential- or time-dependent IR spectra were collected, by which the intermediate process of aqueous electrochemical reduction of CO₂ to CO and CH₄ on FeTAPP was monitored. It was uncovered that coupled with first-electron reduction of [Fe^{II}TAPP]⁰, the porphyrin nitrogen was protonated as the observation of NH⁺ ammonium band in IR spectra, which avoided the formation of Fe–H structure for proton reduction. Most significantly, the role of proton transfer during the CO₂ reduction was revealed by the kinetic isotope spectral investigation: the observed inverse kinetic isotope effect (KIE (H/D)= 0.59) demonstrated that the CO₂ reduction to *COOH is the rate-determining-step of CO₂ reduction to CO on [Fe^{II}TAPP]⁰, and proceeds in a more efficient way as a proton-coupled electron transfer (PCET) process to avoid the formation of charged intermediates with high activation energy. Therefore, the protonated porphyrin-N would be the key to achieve such PCET progress, it acts as a proton relay for the efficient inner-sphere proton transfer to the activated CO₂ molecules. For the reduction above CO, such efficient proton transfer also facilitates the formation of *CHO, the key intermediate for CH₄ generation, this is the first observation of an intermediate of a molecular catalyst in aqueous electrochemical CO₂-to-CH₄ reaction. This work experimentally reveals the role of the reduced porphyrin ligand as proton shuttle to facilitate CO₂ reduction for the first time and should benefit the design of the catalyst of high CO₂ reduction selectivity in aqueous media through the tuning of proton transfer.

2. Experimental section

2.1. Chemicals

The catalysts Iron(III) 5,10,15,20-tetra(4'-N,N,N-Trimethylanilinium)porphyrin pentachloride (FeTAPP, >95%) and the non-metal ligands meso-tetra(4-N,N,N-trimethylanilinium)porphine tetrachloride (H₂TAPP, >95%) were purchased from Frontier Scientific. The electrolytes sodium chloride (NaCl, 99.99%), sodium bicarbonate (NaHCO₃, 99.99%), sodium carbonate anhydrous (Na₂CO₃, 99.99%) were purchased from Macklin, and ¹³C isotopic form sodium bicarbonate-¹³C (NaH¹³CO₃, 99 atom% ¹³C), sodium carbonate-¹³C (Na₂¹³CO₃, 99 atom%

¹³C) were purchased from Sigma-Aldrich. Argon gas (99.999%) were purchased from Beijing Zhongke Tailong Electronic Technology Co., Ltd. Carbon dioxide (99.999%) and carbon monoxide (99.995%) was purchased from Beijing Huanyu Jinghui Jingcheng Gas Technology Co., Ltd. Deuterium oxide (D, 99.96%) and ¹³CO₂ (¹³C, 99%) were purchased from Cambridge Isotope Laboratories. Deuterium chloride (20 wt% solution in D₂O, 99.96 atom% D), sodium deuterioxide (40 wt% solution in D₂O, 99.0 atom% D) were purchased from Acros. All chemicals were used as received without further purification. Ultrapure water was obtained by Millipore (Milli-RO Plus) and employed throughout the experiments.

2.2. Electrochemical measurements

The experiments were carried out in a customized gas-tight H-cell separated by a proton exchange membrane (DuPont Nafion117), working electrode was a 3-mm-diameter glassy carbon disk electrode or a 10 × 10 × 1 mm glassy carbon sheet for cyclic voltammograms (CV) or controlled potential electrolysis (CPE), respectively. A platinum foil (10 × 10 mm) and a Ag/AgCl electrode (3.5 M KCl) were used as counter and reference electrode. The electrolyte employed was 0.1 M NaHCO₃, before measurement, the electrolyte was purged with CO₂ gas for 30 min and the pH of the CO₂-saturated electrolyte was 6.8. For the controlled experiment free of CO₂, the electrolyte was 0.1 M NaCl and the pH was also adjusted to be 6.8 with additional HCl or NaOH (D isotopic experiments are carried out with corresponding deuterium reagents). The electrolysis was controlled by the CHI760E electrochemical workstation, i-R drop was corrected by the automatic compensation mode of the potentiostat, the potentials were all relative to Ag/AgCl without special instructions. After 30-minute electrolysis, the gas products from the headspace were injected into a gas chromatography (Fuli GC-9790, FID with 5 Å molecular column for CO and CH₄, TCD with packed column (TDX-01) for H₂), the liquid products (e.g., formic acid) were detected by an ionic chromatography (Thermal ICS-900, Dionex IonPac AS18).

2.3. In-situ FT-IR measurements

A home-made electro-chemical cell upon Bruker A530/V reflection unit (with CaF₂ crystal as IR window) was equipped on a Bruker Vertex 70 V FT-IR spectrometer with a narrow-band HgCdTe detector. The platinum wire and Ag/AgCl (3.5 M KCl) was employed as counter and reference electrode, respectively, while glassy carbon worked as both the working electrode and reflection plane of the IR detection beam. A micrometer caliper was used to concisely control the distance between the glassy carbon and CaF₂ crystal, the detailed structure of the external reflection IR accessory will be discussed below. The CHI potentiostat was directly triggered by the rapid-scan mode of the FT-IR spectrometer, therefore, the IR data collection was synchronized with the electrochemical scan for either linear sweep voltammetry (LSV) or chronoamperometry (i-t). Each rapid-scan IR spectrum was collected with a spectral resolution of 4 cm⁻¹ and scanning velocity of 160 Hz.

3. Results and discussion

3.1. Instrumental set-up for the electrochemical rapid-scan FT-IR spectroscopy

Owing the particular sensitivity to C–O related species, the in-situ infrared spectroscopy becomes one of the most exploited approaches for the structural identification of CO₂ reduction intermediates [23]. However, the application of in situ FT-IR in aqueous CO₂ reduction is confronted with the critical challenge that the strong absorption of solvent water in the mid-infrared region can easily overwhelm signals from the catalytic system, as the saturated absorption optical path of water is only about 25 μm in aqueous. For the in situ electrochemical IR measurement (EC-IR), two types of set-ups can be applied: the

attenuated total reflection (ATR) mode (Fig. 1a) and the external reflection mode (Fig. 1b). [24].

ATR mode has been more frequently exploited in the aqueous system, in which a thin metal film deposited on an IR transparent prism with high refractive index is used as the working electrode, the IR beam is totally reflected at the interface, but a standing wave generates on the surface of the crystal can penetrate the electrolyte with a depth around several microns [25]. The $\sim\mu\text{m}$ penetration depth in ATR mode naturally avoids the IR-adsorption-saturation by water, making it more frequently exploited in aqueous system. However, the drawback of this mode is that the preparation of working electrodes is required to deposit a thin metal film (Au or Cu) upon ATR crystal (mostly silicon), [26] such electrodes are not inert for either CO_2 reduction or proton reduction (e.g., gold is particularly marked for the high activity to reduce CO_2 into CO) [27]. Therefore, ATR-IR cannot be adopted to a molecular catalytic system where an inert electrode like glassy carbon is required, which guarantees the effective electron transfer to the molecular from the electrode rather than the initiation of the CO_2 reduction directly on the electrode [28]. In contrast, in the external reflection mode, the IR beam passes through the optical window and crosses a very thin layer, then reflects at a flat electrode surface, so the use of glassy carbon electrode is feasible under this mode. Kubiak et al. has previously proceeded such a spectroscopic approach to in-situ monitor the CO_2 reduction on a Mn bipyridine complex in acetonitrile with an optically transparent thin-layer electrode (OTTLE) cell (with an optical path around 300 μm) [29]. However, for the further extension of this IR mode to aqueous system, the distance between the electrode and IR crystal should be deliberately controlled to avoid the IR adsorption saturation by the excessive solvent water.

Herein, a home-made electrochemical IR reflection unit is employed (Fig. 1c and Fig. S1): the polyetheretherketone (PEEK) main body of electrochemical cell and the CaF_2 hemispherical window are sealed with a chemical resistant flat gasket to prevent the leakage of electrolyte and be isolated from the evacuated sample chamber of spectrometer. The glassy carbon electrode can be vertically moved to adjust the vertical distance between the glassy carbon and CaF_2 window, for a more accurate adjustment, a micrometer caliper is set on the top of the glassy carbon electrode. In each measurement, the glassy carbon electrode is pressed against the flat side of a hemispherical CaF_2 window to form a thin electrolyte layer. The details of the distance adjustment for the optimized IR signal are described in the Supporting information (Fig. S2). The optimized vertical distance between the glassy carbon and

CaF_2 crystal is determined to be $\sim 5 \mu\text{m}$, which keeps the whole IR region from 4000 to 1200 cm^{-1} open for measurement in the presence of water solvent. Owing to the small distance of $\sim 5 \mu\text{m}$, the diffusion in the thin layer is largely decoupled with the bulk solution, [30] thus, such an IR set-up provides a full-vision monitoring of reaction procedure that not only the molecular catalysts and their intermediates adsorbed on the electron surface, but also the ones released from the surface are now within the scope of IR spectroscopy [28]. In another aspect, owing to the relatively sealed system of the thin layer that limits the exchange of electrolyte with the bulk solution, the recorded variations in the concentration of CO_2 (or carbonic acid) and its deprotonated form like HCO_3^- and CO_3^{2-} in IR spectra, become more meaningful in tracing the release and transfer of protons.

In electrochemical IR measurement, the accurately correlating the recorded IR spectrum with the bias applied is of particular significance. To minimizing the delay between the start of potentiostat and IR spectrometer, in rapid-scan mode, we directly trigger the potentiostat by the low out-put signal sent from the spectrometer. The delay in the start of potentiostat is therefore less than 1 ms, leading to a precise synchronization between electrolysis and IR data acquisition. Since the maximum time-resolution of our rapid-scan FT-IR is 60 ms, such synchronization guarantees the accuracy in the spectral kinetic analysis like the correspondence of the evolution or decay of the intermediates to the bias applied and the correlation between intermediates and the variation of $\text{CO}_2/\text{HCO}_3^-/\text{CO}_3^{2-}$, which are specifically focused in this work.

3.2. Activity test of the aqueous electrochemical CO_2 reduction on FeTAPP

Before the in-situ FT-IR studies, the performance of electrochemical CO_2 reduction on FeTAPP in aqueous system was first re-examined and compared with that reported in literatures. The cyclic voltammogram (CV) measurements was performed both in the absence (Ar-purged 0.1 M NaCl) and presence of CO_2 (CO_2 saturated 0.1 M NaHCO_3) at identical pH of 6.8 (Fig. 2a). It should be noted that the pH of CO_2 saturated 0.1 M HCO_3^- aqueous solution is 6.8, while in the absence of CO_2 , the pH is approximately 8.3, if the pH of 0.1 M HCO_3^- is adjusted to 6.8 by HCl solution, bicarbonate will release CO_2 via the fast equilibrium ($\text{HCO}_3^- + \text{H}^+ \rightarrow \text{CO}_2 + \text{H}_2\text{O}$), and the control system cannot be still regarded as a CO_2 -free system. For the ease of description and visually showing the reducing state of the molecular catalyst, we use $[\text{FeTAPP}]^x$ to represent the intermediates in different stages from the reduction of

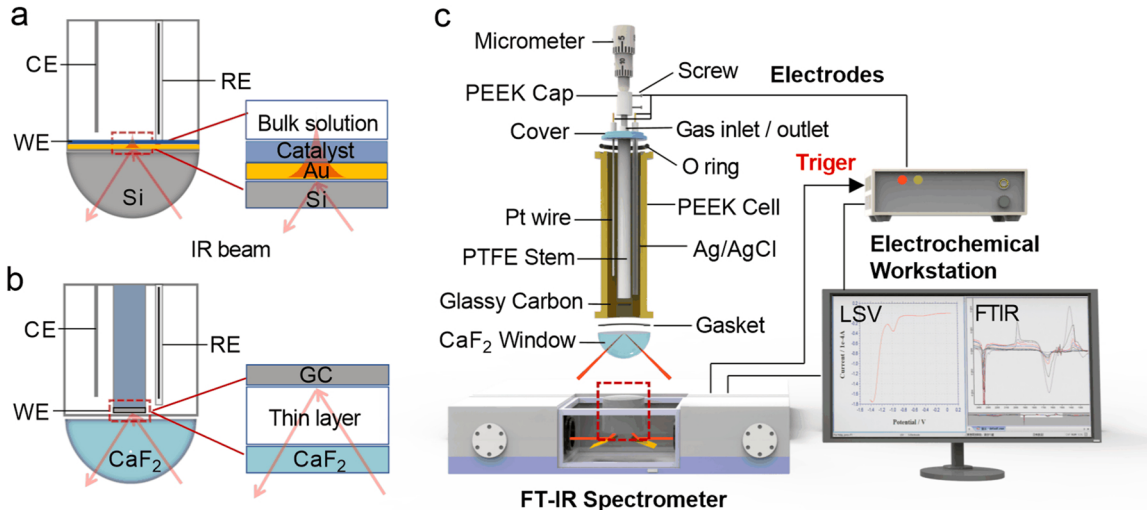


Fig. 1. The schemes for the electrochemical IR spectroscopy in (a) attenuated total reflection (ATR) mode and (b) external reflection mode. (c) The instrumental set-up of rapid-scan FT-IR spectroscopy in external reflection mode. The configuration of homemade electrochemical cell simplified in the red dashed box is shown above the spectrometer.

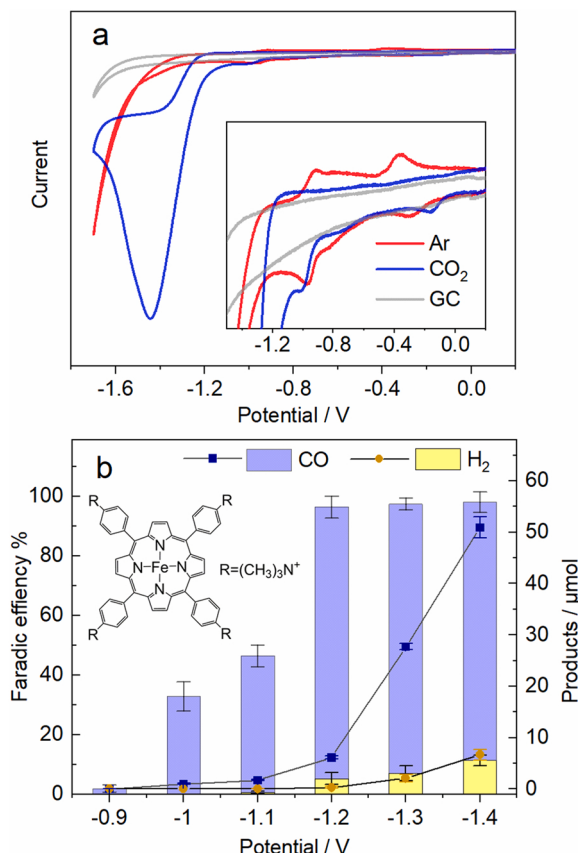


Fig. 2. (a) The cyclic voltammetry of $[\text{Fe}^{\text{III}}\text{TAPP}]^+$ in aqueous media under atmosphere of Ar (red) or CO_2 (blue). The CV scan was between +0.2 V and -1.7 V (vs Ag/AgCl) at a scan rate of $100 \text{ mV}\cdot\text{s}^{-1}$. Blank experiment was conducted on glassy carbon without molecular catalyst under Ar (light gray). The inset shows the enlarged region of reductive waves before the catalytic current is initiated. (b) The H_2 (yellow) and CO (blue) production (line + symbol, right Y axis) and corresponding Faradic efficiency (column, left Y axis) on FeTAPP under bias ranging from -0.9 to -1.4 V (vs Ag/AgCl). The inset shows the molecular structure of FeTAPP, $\text{R} = (\text{CH}_3)_3\text{N}^+$.

$[\text{Fe}^{\text{II}}\text{TAPP}]^0$, for instance, the one-electron reduced intermediate from $[\text{Fe}^{\text{II}}\text{TAPP}]^0$ is denoted as $[\text{FeTAPP}]^-$, while the two-electron reduced one is $[\text{FeTAPP}]^{2-}$. The CV scan was started from $[\text{Fe}^{\text{III}}\text{TAPP}]^+$. In the absence of CO_2 , the first reductive wave appeared at -0.29 V (vs. Ag/AgCl), since no noticeable wave was observed in metal-free porphyrin ligand (H_2TAPP) in this potential range (Fig. S3), we assigned this wave to the reduction of $[\text{Fe}^{\text{III}}\text{TAPP}]^+$ to $[\text{Fe}^{\text{II}}\text{TAPP}]^0$ [13,22]. With the bias going more negative, two consecutive one-electron reduction processes were identified with the observation of two neighboring waves at -0.82 and -0.97 V. In the reverse scan, a quasi-reversible oxidation wave appeared at -0.91 V followed by a shoulder at -0.79 V. No prominent water reduction was observed until the potential reached -1.24 V. Therefore, we assigned these two reduction waves to the one- and two-electron reduction of $[\text{Fe}^{\text{II}}\text{TAPP}]^0$ to $[\text{FeTAPP}]^-$ and $[\text{FeTAPP}]^{2-}$, respectively. In CO_2 saturated electrolyte, the similar three reduction waves appeared at -0.16, -0.77 and -1.06 V, respectively. The significant catalytic CO_2 reduction current occurred immediately after the peak of the third reductive wave, which was about 200 mV more positive than on-set potential of water reduction under Ar, demonstrating the preferable CO_2 reduction than water reduction on FeTAPP.

Then preparative-scale controlled potential electrolysis (CPE) were conducted in CO_2 -saturated 0.1 M NaHCO_3 . Gas and liquid products generated at the CPE was analyzed by gas chromatography and ion chromatography separately after 30-minute electrolysis. As shown in Fig. 2b, in consensus with CV results, no significant evolution of CO was

obtained until the bias reached -1.2 V, in which potential the Faradic efficiency (FE) of CO_2 reduction reached 91.2% in contrast of only 5.2% for of H_2 production, no detectable liquid products like formic acid were observed in ion chromatography. When the CO evolution became more robust at -1.3 and -1.4 V, FE of CO_2 reduction kept above 90%. It is also worth noting that a small amount of CH_4 was detected in gas chromatography at -1.4 V (Fig. S4). In conclusion, FeTAPP molecular catalyst exhibited an almost exclusive CO_2 -to-CO reduction in aqueous media, this result is in accordance with literature reports [22]. Therefore, the spectroscopic studies can then be conducted in the present reaction conditions to explore the origin of the highly selective CO_2 reduction capability on FeTAPP molecular catalyst.

3.3. The rapid-scan FT-IR studies of electrochemical CO_2 reduction on FeTAPP

3.3.1. The reduction of $[\text{Fe}^{\text{II}}\text{TAPP}]^0$ in absence of CO_2

A control experiment to investigate the reduction of FeTAPP in absence of CO_2 was conducted in 0.1 M NaCl (pH 6.8) under Ar atmosphere. It is generally recognized that the CO_2 reduction on FeTAPP (or other Fe-porphyrin) is initiated from $[\text{Fe}^{\text{II}}\text{TAPP}]^0$ [31]. Before the LSV scan, an electrolysis at -0.1 V for 5 min was first conducted to completely convert $[\text{Fe}^{\text{III}}\text{TAPP}]^+$ into $[\text{Fe}^{\text{II}}\text{TAPP}]^0$ in the thin layer between the electrode and CaF_2 window, and the background IR spectrum collected after electrolysis contained only $[\text{Fe}^{\text{II}}\text{TAPP}]^0$. The LSV scan range was from -0.22 to -1.42 V (vs Ag/AgCl) in the rate of $2.5 \text{ mV}\cdot\text{s}^{-1}$, while each corresponding in-situ IR spectrum was collected in a potential range of 15 mV. The LSV collected in a relatively sealed thin layer in the external reflection IR cell is in some part differential with that in the open systems as Fig. 2a, not only owing to the slower scan rate to match the IR spectra collection, but also the limited reagents in the thin liquid layer and the impeded substance supplement from the outside electrolyte, which led to a rapid depletion of reagents during the electrochemical scan and enabled the neighboring reductive waves being more resolvable. As shown in Fig. 3a, at the similar potential range for the generation of $[\text{FeTAPP}]^-$ and $[\text{FeTAPP}]^{2-}$ in Fig. 2a, two more resolvable peaks were observed at -0.76 and -0.95 V, respectively. The ratio of the integrated areas for the two reductive waves was 0.89 close to 1, confirming the successive one-electron reduction from $[\text{Fe}^{\text{II}}\text{TAPP}]^0$ to $[\text{FeTAPP}]^-$ and subsequent $[\text{FeTAPP}]^{2-}$ upon these two reductive waves.

When checking the synchronized in-situ IR spectra, two sets of IR bands were observed at the corresponding bias. As shown in Fig. 3c, the IR bands for $[\text{FeTAPP}]^-$ became visible at around -0.60 V: in C=C vibration region of $\sim 1500 \text{ cm}^{-1}$, [32,33] the growth at 1523, 1507 and 1485 cm^{-1} were observed together with the decrease at 1532 and 1497 cm^{-1} , in C-N vibration region of $\sim 1300 \text{ cm}^{-1}$, [34,35] the appearance of 1331 cm^{-1} band was accompanied with the decay at 1340 cm^{-1} , indicating the conversion of $[\text{Fe}^{\text{II}}\text{TAPP}]^0$ to $[\text{FeTAPP}]^-$. When bias over -0.90 V, the IR feature in C=C vibration region altered: with the negative bands at 1532 and 1497 cm^{-1} remained, the newly raised band was centered at 1513 cm^{-1} , which was clearly recognized in trace (i) in Fig. 3c. More significant alternation was observed in C-N vibration region: the new band appeared at higher wavenumbers of 1357 cm^{-1} . These new bands were assigned to the two-electron reduced $[\text{FeTAPP}]^{2-}$, and at -1.35 V when the catalytic current for water reduction was already significant, the IR bands for $[\text{FeTAPP}]^{2-}$ were still visible, suggesting a much faster recovery of $[\text{FeTAPP}]^{2-}$ than its consumption during the water reduction, in another word, in near-neutral conditions, the water reduction initiated from $[\text{FeTAPP}]^{2-}$ is very sluggish.

3.3.2. The first-electron reduction of $[\text{Fe}^{\text{II}}\text{TAPP}]^0$ in the presence of CO_2

Then the CO_2 reduction on $[\text{Fe}^{\text{II}}\text{TAPP}]^0$ was monitored in CO_2 saturated 0.1 M NaHCO_3 solution by the identical IR methodology. One of the major differences for the IR spectra collected under $\text{CO}_2/\text{HCO}_3^-$

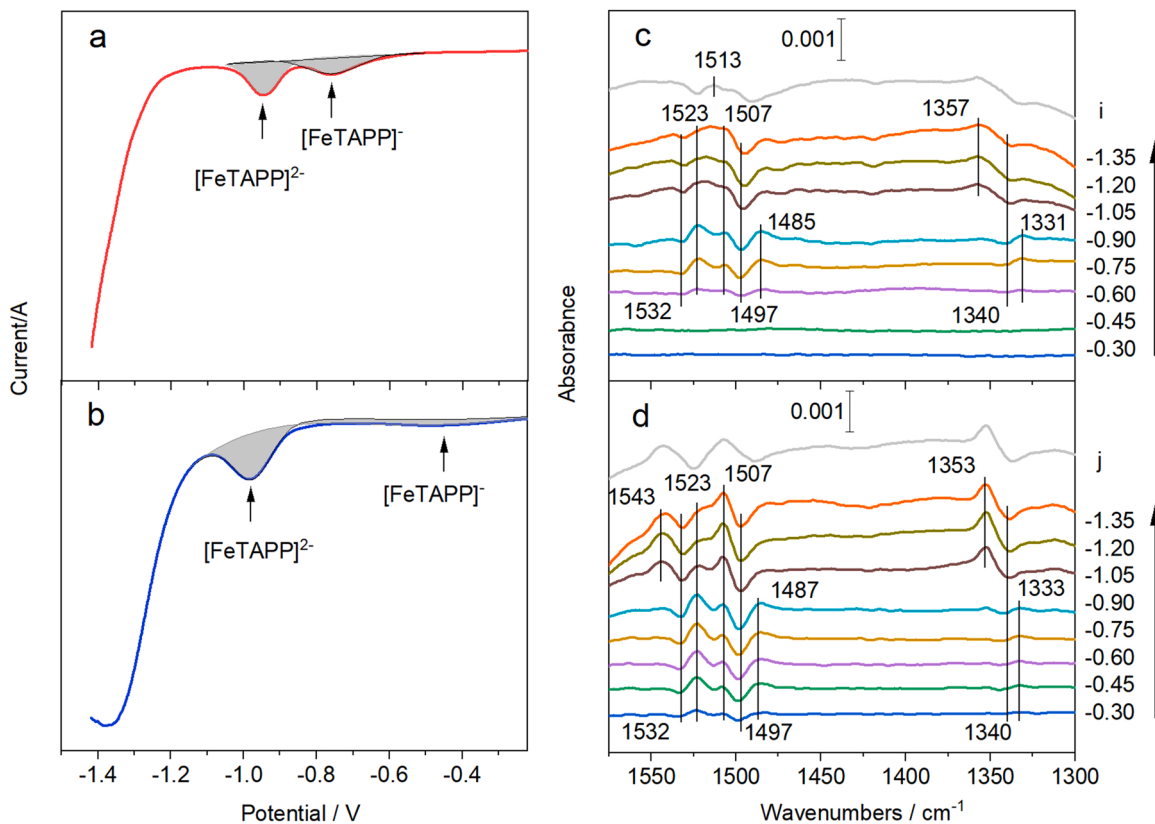


Fig. 3. The linear scan voltammetry (LSV) curve and corresponding potential-dependent in-situ IR spectra of FeTAPP under atmosphere of Ar (a and c) and CO₂ (b and d), respectively. Before the LSV scan, the system was electrolysis at -0.1 V for 5 min, the background was collected just before the LSV scan. The trace (i) in (c) and (j) in (d) display the difference spectrum between the two collected at -0.90 V and -1.20 V.

comparing with that under Ar was the remarkable variation in HCO₃²⁻/CO₃²⁻ bands that would shield the IR bands of reductive intermediates in the wavenumbers of 1575–1300 cm⁻¹. To precisely compare the reductive intermediates of FeTAPP generated under CO₂ and Ar, we displayed the IR spectra collected under CO₂/HCO₃²⁻ in two manners: one was the raw data shown in Fig. 4c, the other one was with HCO₃²⁻/CO₃²⁻ bands deducted to open the IR region from 1550 to 1300 cm⁻¹ shown in Fig. 3d (the detailed procedure to deduct HCO₃²⁻/CO₃²⁻ bands was shown in Figs. S5,6). For the first-electron reduction of [Fe^{II}TAPP]⁰ under CO₂/HCO₃²⁻, as LSV shown in Fig. 3b, the reduction wave for [Fe^{II}TAPP]⁰ to

[FeTAPP][·] became very broad and the center of which positively shifted approximately 0.3 V. Correspondingly, in IR spectra (Fig. 3d), the set of IR bands that were almost identical to [FeTAPP][·] can also be observed 0.3 V earlier than that under Ar. Furthermore, it was confirmed that during the one-electron reduction of [Fe^{II}TAPP]⁰, CO₂ molecules were not activated by the molecular catalyst. If the linear CO₂ molecular was activated and adsorbed on [FeTAPP][·], it should be bent to display the O-C-O stretching vibration band visible in the region of 1700–1200 cm⁻¹, [17] but such band was absent before the CO bond intermediate appeared at 1966 cm⁻¹ in the sub-second time scale

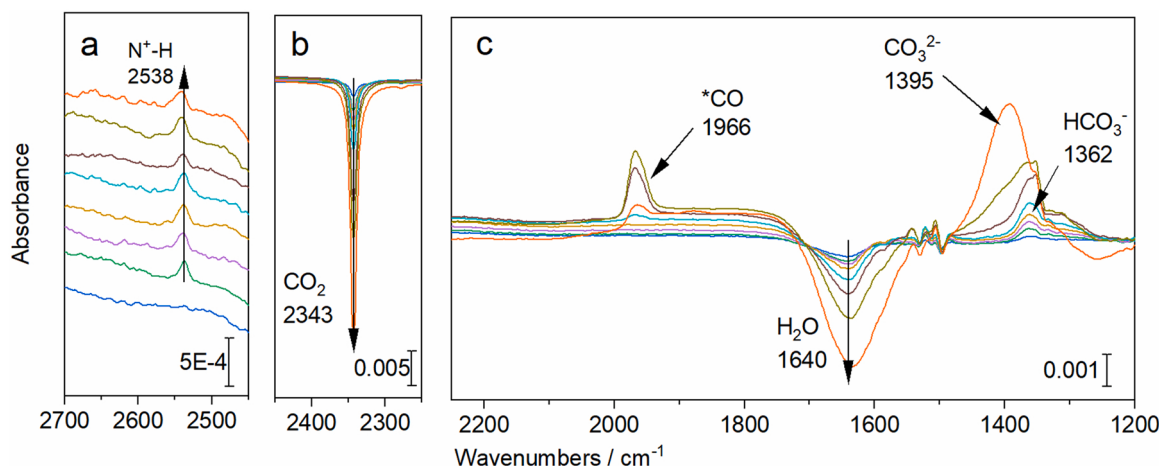


Fig. 4. Potential-dependent in-situ IR spectra of FeTAPP under CO₂-saturated NaHCO₃ electrolyte in the range of (a) 2700 ~ 2450, (b) 2450 ~ 2250, (c) 2250 ~ 1200 cm⁻¹. The potential of LSV was scanned from -0.22 V to -1.42 V at a rate of 2.5 mV s⁻¹. Before the LSV scan, the system was electrolysis at -0.1 V for 5 min, the background was collected just before the LSV scan.

(Fig. S7). Also, when using $^{13}\text{CO}_2/\text{H}^{13}\text{CO}_3^-$ instead of their ^{12}C -counters, no IR band for the intermediates exhibited the $^{13}\text{C}/^{12}\text{C}$ isotope shift (Fig. S8).

When checking the raw data containing $\text{HCO}_3^-/\text{CO}_3^{2-}$ bands (Fig. 4a-c), it became intriguing to discover that even no CO_2 activation occurred during the first-electron reduction, the decrease of the free CO_2 band at 2343 cm^{-1} was observed (Fig. 4b). Noteworthy, accompanied with the depletion of free CO_2 was the decay in H–O–H scissor vibration of water at 1640 cm^{-1} , the growth of HCO_3^- band at 1362 cm^{-1} and appearance of a new band at 2538 cm^{-1} (Fig. 4a). As known to all, CO_2 molecules are ionized in water and form the equilibrium of $\text{CO}_2 + \text{H}_2\text{O} \leftrightarrow \text{HCO}_3^- + \text{H}^+$, [27] it seems that the consumption of CO_2 was originated from the right-shifting of the equilibrium. Since no H_2 production was observed in this potential range, the most possible approach to consume H^+ and afterward shift the ionization equilibrium should be the protonation of $[\text{FeTAPP}]^-$. The coupled protonation during electron-reduction as the so-called proton-coupled electron transfer (PCET) is recognized to notably reduce the energy barrier during the electron transfer, which explains the positively shifted reductive potential for $[\text{Fe}^{\text{II}}\text{TAPP}]^0$ to $[\text{FeTAPP}]^-$ under $\text{CO}_2/\text{HCO}_3^-$ comparing to that under Ar in near-neutral condition. Although the initial pH in $\text{CO}_2/\text{HCO}_3^-$ electrolyte was also near-neutral and identical to that in Ar/ Cl^- , the dissolved CO_2 (carbonic acid) acted as a pool of protons to gradually release proton that facilitated the protonation of $[\text{FeTAPP}]^-$. Precisely because of the proton source from the gradual ionization of CO_2 , the instant concentration of protons was not high enough to reductively deplete all the $[\text{Fe}^{\text{II}}\text{TAPP}]^0$ molecules in the thin liquid layer via a PCET procedure, resulting in a prolonged reduction procedure to adapt to the slow release of protons from the ionization, as the observed broadened reductive wave in Fig. 3b.

Then it is critical to determine the location of protonation on $[\text{FeTAPP}]^-$ whether on Fe center or porphyrin ligand. Porphyrin-based ligand is characterized as redox-noninnocent, [36] therefore, during the reduction of metal-porphyrin, the incoming electrons can be localized on the metal center or the ligand, and the electron distributions are strongly dependent on the properties of both metal center and the ligand [11]. The location for trapping the reducing electron significantly affects the electrophilic attack of both H^+ and CO_2 , leading to distinctive distributions of reducing products, for instance, the attack of proton to the reduced metal center would result in the formation of H_2 [16]. Herein, for the possibility of protonation on Fe center, firstly, no IR band that can be possibly assigned to Fe–H species was observed. Moreover, if Fe–H structure was formed, there should be a partial electron transfer from Fe center to H^+ , which led to the alternation in the electron density distributions in $[\text{FeTAPP}]^-$ moiety and thereafter the variations in the IR bands for C=C and C–N vibrations, such variations were not monitored here. In the other hand, it is worth noting that TAPP contains four strong electron-withdrawing groups of trimethylanilinium, which makes the ligand easier to be reduced: a recent theoretical calculation by Liao et al. predicted that during the reduction from $[\text{Fe}^{\text{II}}\text{TAPP}]^0$ to $[\text{FeTAPP}]^-$, the reduction and protonation were both localized on TAPP ligand, and the activation energy for the formation of $[\text{FeTAPP}]^-$ with protonation on pyrrole-N of TAPP (noted as $[\text{Fe}(\text{TAPP}-\text{H}^+)]^0$) was 0.16 eV lower than unprotonated $[\text{FeTAPP}]^-$, [15] which is accordant with the our observation in LSV. Noteworthy, synchronized with the depletion of free CO_2 and the growth of HCO_3^- was the appearance of a new weak band at 2538 cm^{-1} (Fig. 4a), while this band was invisible during the electrolysis in the absence of CO_2 (Fig. S9). Generally, the N–H stretching vibration for tertiary ammonium is in the frequency of $2700 \sim 2400\text{ cm}^{-1}$, [37–39] we also conducted an acidification on $[\text{Fe}^{\text{III}}\text{TAPP}]^+$ with the addition of 0.1 M HCl, a close band at 2561 cm^{-1} emerged with the decrease of pH (Fig. S10). Therefore, we identified the 2538 cm^{-1} band as NH^+ ammonium on the protonated TAPP ligand. To be concluded, owing to the presence of CO_2 (or carbonic acid) as pool of protons to gradually release protons, a protonation in TAPP ligand occurred simultaneously with the first-electron reduction of $[\text{Fe}^{\text{II}}\text{TAPP}]^0$.

3.3.3. The second-electron reduction of $[\text{Fe}^{\text{II}}\text{TAPP}]^0$ and the generation of CO

When the bias reached around -0.90 V , in which potential $[\text{FeTAPP}]^{2-}$ was monitored in the absence of CO_2 (Fig. 3c), the observation of an evident band at 1966 cm^{-1} for trapped CO consolidated the completion of the two-electron reduction of CO_2 to CO by $[\text{FeTAPP}]^{2-}$ (Fig. 4c). Simultaneous with the generation of CO, the two-electron reduced $[\text{FeTAPP}]^{2-}$ was recovered to $[\text{Fe}^{\text{II}}\text{TAPP}]^0$ and subsequently trapped the in-situ generated CO, exhibiting a red-shifted IR frequency than the free CO (2170 cm^{-1}) [18,40]. However, what we monitored in IR spectra was not simply $[\text{Fe}^{\text{II}}(\text{CO})\text{TAPP}]^0$, since at this potential, the recovered $[\text{Fe}^{\text{II}}\text{TAPP}]^0$ moiety can be instantly reduced again while keeping CO trapped. The evidence was that in LSV (Fig. 3b), the integrated area for the second reductive wave was almost twice of that for the first one (1:0.54), suggesting a two-electron reduction upon this reduction wave, and $[\text{Fe}^{\text{II}}(\text{CO})\text{TAPP}]^0$ should be further one-electron reduced. When deducting the CO_3^{2-} and HCO_3^- bands (Fig. 3d), the IR bands at 1543 and 1353 cm^{-1} for the variation in TAPP ligand consolidated the reduction in $[\text{Fe}^{\text{II}}\text{TAPP}]^0$ moiety. It is also worth noting that the ammonium band at 2538 cm^{-1} kept almost unchanged during the second reduction wave (Fig. 4a), demonstrating the protonation of the TAPP ligand simultaneously with the reduction. Therefore, the stable FeTAPP species observed upon the second reduction wave is in the form of $[\text{Fe}^{\text{II}}(\text{CO})(\text{TAPP}-\text{H}^+)]^0$. Up to Now, species observed in spectra generated in the first and second reduction stage were all identified, summary of IR bands and related intermediates were listed in Table 1.

It is intriguing to discover that at the potential range of the second reduction wave, the generation of CO was more likely a stoichiometric reaction rather than a catalytic one. The robust catalytic current of CO_2 reduction occurred at the end of second reduction when the significant generation of gaseous CO can be monitored in gas chromatography (Fig. 2b). Also, no decay in the intensity of trapped CO (1966 cm^{-1}) was observed until the bias reached -1.20 V . The trapping of CO on $[\text{Fe}^{\text{II}}(\text{CO})(\text{TAPP}-\text{H}^+)]^0$ was very stable and blocked the catalytic site for the recycled reactions, a more negative bias was therefore necessary for the desorption of CO and the initiation of the catalytic CO_2 reduction.

The kinetics of CO_2 consumption and $\text{HCO}_3^-/\text{CO}_3^{2-}$ generation in LSV scan (Fig. 5) provided extra evidence to propose the reaction pathway of CO_2 reduction to CO on FeTAPP. Since the cycling the FeTAPP was not conducted until the end of the second reduction wave, the reduction of FeTAPP and its subsequent reaction with CO_2 was stoichiometric in such bias range. It can be calculated that the consumption of CO_2 in the second reduction stage at -0.9 V was nearly twice of that in the first reduction stage at -0.3 V (Fig. S11). Upon the first reduction stage, as discussed above, the role of CO_2 was to ionize with water to provide H^+ for the protonation of the reduced ligand (Eq. 1). During the second reduction stage, one half of CO_2 was stoichiometrically reacted with $[\text{FeTAPP}]^{2-}$ for the generation of $[\text{Fe}^{\text{II}}(\text{CO})\text{TAPP}]^0$ (Eq. 2), for the other half, as the observation of ammonium band in IR spectra, this part of CO_2 should still play role as proton source (Eq. 3). The synchronized increase of HCO_3^- with the consumption of CO_2 in first reduction stage

Table 1
IR frequencies of reductive intermediates of $[\text{Fe}^{\text{II}}\text{TAPP}]^0$ in the presence and absence of CO_2 .

	Bias ^a	n (e ⁻) ^b	Wavenumbers / cm^{-1}
$[\text{Fe}^{\text{II}}\text{TAPP}]^0$		0	1532, 1497, 1340
0.1 M NaCl / Ar			
$[\text{FeTAPP}]^-$	-0.52	1	1523, 1507, 1485, 1331
$[\text{FeTAPP}]^{2-}$	-0.85	2	1513, 1357
0.1 M NaHCO_3 / CO_2			
$[\text{Fe}(\text{TAPP}-\text{H}^+)]^0$	-0.22	1	2538, 1523, 1507, 1487, 1333
$[\text{Fe}^{\text{II}}(\text{CO})(\text{TAPP}-\text{H}^+)]^0$	-0.85	3	2538, 1966, 1543, 1353

^a The set-on potential for the appearance of the intermediate IR bands (vs Ag/AgCl).

^b The number of electrons transferred to $[\text{Fe}^{\text{II}}\text{TAPP}]^0$.

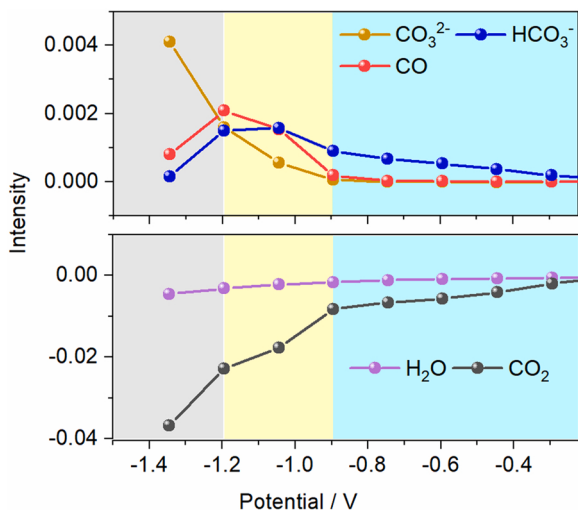
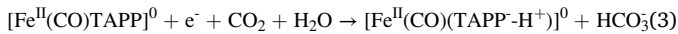
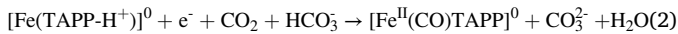


Fig. 5. The potential-dependent kinetics (Top) growth of HCO₃ (1362 cm⁻¹), CO₃²⁻ (1395 cm⁻¹), CO (1966 cm⁻¹) bands and (Bottom) decline of H₂O (1640 cm⁻¹), CO₂ (2343 cm⁻¹) bands. The three reduced stages are shown in (I) cyan (-0.22 V~ -0.9 V), (II) yellow (-0.9 V~ -1.2 V) and (III) gray (-1.2 V~), respectively.

consolidated the proton release by shifting the ionization equilibrium of CO₂/H₂O, whereas, in the second reduction stage, the growth of HCO₃ became slower, instead, the robust of generation of CO₃²⁻ was observed, suggesting the conversion of HCO₃ to CO₃²⁻. In the first reduction stage of the catalyst, [Fe^{II}TAPP]⁰ goes on a PCET pathway to form [Fe(TAPP-H⁺)]⁰ with the protonation of porphyrin ring, which consumes dissolved CO₂ but accumulates HCO₃ around the catalysts. It should be noted that the TAPP ligand contains four positively charged $-\text{N}(\text{CH}_3)_3^+$ groups, therefore, HCO₃ can be the outer-sphere anion attracted by Columbian force. Such outer-sphere HCO₃ can also be the proton source for CO₂ reduction that was converted to CO₃²⁻ after providing the proton. When the bias became more negative to achieve the desorption of CO and recycling of the catalyst, the IR bands for HCO₃ began to decrease and the total increment gradually returned to 0, the net reaction of CO₂ reduction on FeTAPP, according to the kinetics of CO₂ and CO₃²⁻, was 2CO₂ + 2e⁻ → CO + CO₃²⁻.



3.3.4. The inverse kinetic isotope (H/D) effect in CO generation

Now the only missing piece of the in-situ FT-IR measurements is the observation and identification of intermediates before C–O cleavage, however, the reaction rate of CO₂-to-CO seems to be faster than the time-resolution of our rapid-scan FT-IR. To gain more insights into this fast process, we make efforts to study the dynamics of these ‘missing’ intermediates via the kinetic isotope spectral analysis. For the CO₂ reduction to CO on molecular catalyst, the well-accepted reaction pathway involves the transfer of two electrons and one proton (* stands for the species adsorbed on molecular catalyst): CO₂ (+ e⁻) → *COO⁻ (+ H⁺) → *COOH (+ e⁻) → CO (+ OH⁻) [41]. However, there is still debate in terms of the rate-determining-step (RDS) for this two-electron reduction, which is mostly determined by Tafel analysis, reaction order analysis or theoretical calculation. It should be noted that the transfer of electron and proton may not be stepwise, the proton transfer can be associated with either the first or the second electron transfer, as the so-called proton-coupled electron transfer (PCET), which is more

efficient than the stepwise one by avoiding the charged intermediate with higher activation barrier [6,7]. If the proton is involved in RDS, whether the existence of H/D kinetic isotope effect can be an powerful evidence in revealing the mechanism.

For the kinetic isotope experiment, the in-situ IR spectroscopy was synergistic with the amperometry i-t scan at the potential of -0.9 V (vs Ag/AgCl) to trace the growth kinetic of the trapped CO band at 1966 cm⁻¹, and the experiment was conducted in CO₂ saturated H₂O/HCO₃ and D₂O/DCO₃, respectively. As shown in Fig. 6, within the 60 s electrolysis, the growth of the trapped CO band at 1996 cm⁻¹ was almost linearly with time, following a zero-order growth kinetic. It is discovered that the proton transfer played a critical role in CO generation, as the slope of CO growth in D₂O was observed to be notably sharper than that in H₂O, the zero-order kinetic reaction rates of k_H and k_D were fitted to be 1.17×10^{-5} and $1.99 \times 10^{-5} \text{ s}^{-1}$, respectively, and the kinetic isotope effect (KIE) of k_H/k_D was calculated to be 0.59. A k_H/k_D value < 1 is uncommon and should be indicative of an inverse KIE. Such an inverse KIE excludes the possibility that the conversion of *COOH to CO is the RDS, in which step the proton is associated to the cleaved C–O bond that causes a secondary order KIE with k_H/k_D value in the range of 1–2.[42] Limited causes lead to the occurrence of inverse KIE, one origin results from a change from a less hybridized state to a more hybridized state (e.g., sp² to sp³) [43]. For example, we have previously reported that during the photocatalytic dehalogenation of aromatic halides, the adding of proton to the aromatic ring in a PCET procedure exhibited an inverse KIE of 0.7. Such a change in the hybridization state during the RDS leads to a larger difference in the ΔZPE (zero-point energy) of the transition state than in the ΔZPE in the ground state [44]. Herein, if the first electron reduction of CO₂ is coupled with the proton transfer as the PCET procedure (CO₂ + e⁻ + H⁺ → *COOH), the proton would directly participate in the hybridized state alternation from *CO₂ (sp²) to *COOH (sp³), which should result in the occurrence of inverse KIE as detected. Therefore, the kinetic isotope experiment reveals that the RDS of CO₂ reduction on FeTAPP is the reduction of CO₂ to *COOH, moreover, it proceeds in a more efficient way as a PCET process to avoid the formation of charged intermediates with high activation energy. To achieve such PCET progress, there should be an efficient proton transfer approach on reduced FeTAPP, which is most possibly via the intramolecular proton transfer from the protonated porphyrin ligand.

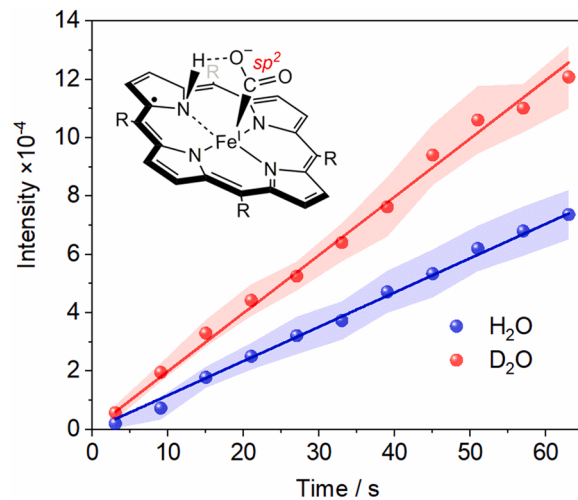


Fig. 6. The quasi-zero-order kinetic for the growth of the trapped CO band (1966 cm⁻¹) within 60 s of electrolysis at -0.9 V and the investigation of its kinetic isotope (H/D) effect. The error area represents the standard deviation of three measurements. The inset shows the possible pathway of nucleophilic attack of CO₂ by FeTAPP, R = (CH₃)₃N⁺.

3.3.5. The reduction of CO₂ above CO

FeTAPP is the only molecular catalyst reported to reduce CO₂ to CH₄ in a homogeneous system, [21] herein, the generation of CH₄ was detected at the bias of -1.4 V. In in-situ FT-IR, when the bias was more negative than -1.2 V, the catalytic current was monitored in LSV, simultaneously, the CO band at 1966 cm^{-1} began to decline (Fig. 7a), indicating the desorption of CO from FeTAPP catalyst and the subsequent recycling of the catalyst. At about -1.2 V when the decline of 1966 cm^{-1} band was significant, two new bands at 1881 and 1783 cm^{-1} became obvious. When using $^{13}\text{CO}_2$ and NaH $^{13}\text{CO}_3$ instead of $^{12}\text{CO}_2$ and NaH $^{12}\text{CO}_3$, the bands at 1966 , 1881 and 1783 cm^{-1} had their ^{13}C count part at 1921 , 1841 and 1745 cm^{-1} , respectively (Fig. 7b), whereas, when replacing H₂O solvent with D₂O, only the 1783 cm^{-1} band red-shifted to 1770 cm^{-1} (Fig. 7c). For CO adsorbed on transient metal center, the d electron of the metal is back-donated to the π anti-orbit of CO, leading to the red-shift of the IR frequency than the free CO [18,40]. Since the 1966 cm^{-1} band was assigned to Fe $^{\text{II}}$ -CO, the 1881 cm^{-1} band without a H/D isotope shift should be CO trapped on reduced Fe $^{\text{I}}$ site, which intensified the back-donation with extra d electron in Fe center. For 1783 cm^{-1} band, the H/D isotope shift was only 13 cm^{-1} , also considering that the bias for the appearance and growth of this band was accordant with the detection of CH₄ in gas chromatography, therefore, it should be from the C=O vibration in *CHO, the intermediate for CH₄ generation [45]. As we all know, this is the first time to observe an intermediate of a molecular catalyst in aqueous electrochemical CO₂-to-CH₄ reaction. The similar experiments were also conducted under CO (Fig. S12). Before electrolysis, the initial [Fe $^{\text{III}}$ TAPP] $^+$ had been converted to [Fe $^{\text{II}}$ (CO)TAPP] 0 at -0.3 V, when the potential reached -1.2 V, a negative band emerged at 1966 cm^{-1} correspond to consumption of [Fe $^{\text{II}}$ (CO)TAPP] 0 , then two positive bands at 1881 and 1770 cm^{-1} appeared, this observation is in agreement with results in Fig. 7c.

The hydrogenation of *CO to *CHO is generally regarded as the key step for CH₄ generation, [46] the competition between hydrogenation and *CO desorption determines the efficiency of CH₄ generation [47]. In hydrogenation that requires coupled electron-proton reaction, it has been proposed that the electron transfer happens on a time-scale much faster than proton transfer, [48] therefore, the efficient proton transfer should be the necessity for *CHO generation. Since the appearance of 1881 and 1783 cm^{-1} bands were synchronized, it can be speculated that the conversion from trapped CO on Fe $^{\text{II}}$ ([Fe $^{\text{II}}$ (CO)(TAPP $^-$ H $^+$)] 0 , at 1966 cm^{-1}) to Fe $^{\text{I}}$ -CO (1881 cm^{-1}) is competitive with that to *CHO (1783 cm^{-1}). Since CO was significantly generated at bias <-1.2 V, the generation of Fe $^{\text{I}}$ -CO would lead to the subsequent release of CO from

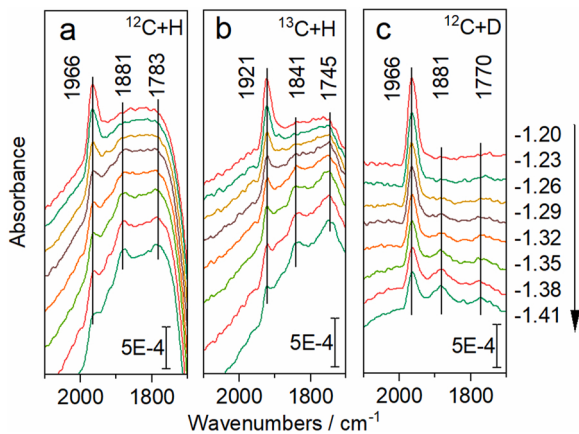
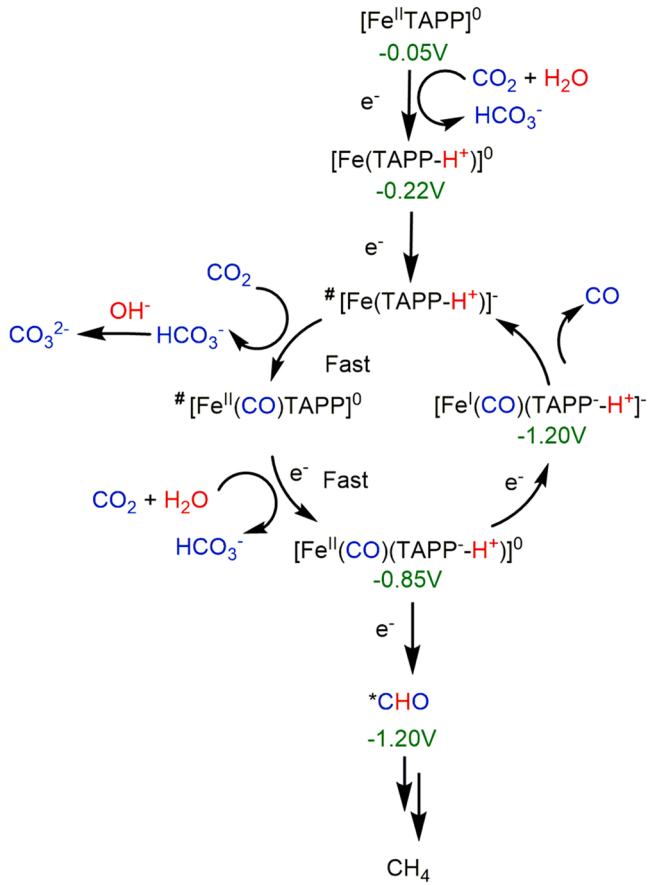


Fig. 7. IR spectra collected above -1.20 V in CO₂-saturated 0.1 M NaHCO₃ aqueous solution with different types of isotope labelling: (a) NaH $^{12}\text{CO}_3$ and $^{12}\text{CO}_2$ in H₂O; (b) NaH $^{13}\text{CO}_3$ and $^{13}\text{CO}_2$ in H₂O (c) NaH $^{12}\text{CO}_3$ and $^{12}\text{CO}_2$ in D₂O. The background spectrum was collected at -0.22 V.

the molecular catalyst and initiated the catalytic reduction of CO₂ to CO. It should be noted that the conversion of [Fe $^{\text{II}}$ (CO)(TAPP $^-$ H $^+$)] 0 was notably involved with protons, as the decline of Fe $^{\text{II}}$ -CO band was much slower in D₂O electrolyte (Fig. 7c). Also, the relative intensity ratio between Fe $^{\text{I}}$ -CO and *CHO was distinctive between H₂O and D₂O, more *CHO was generated in H₂O. Therefore, the proton transfer plays the pivotal role in CH₄ generation, and the specific proton transfer approaches in FeTAPP, as discussed above, should be the origin for the scarcely reported CH₄ generation on FeTAPP.

Based on the in-situ FT-IR studies, the detailed CO₂ reduction pathway on FeTAPP can be now interpreted, as shown in Scheme 1. During the one-electron reduction of [Fe $^{\text{II}}$ TAPP] 0 , the reduction should be mainly localized in TAPP ligand which is recognized as a redox-noninnocent ligand, no nucleophilic attack of proton or activation of CO₂ on Fe center is conducted. The protonation in the reduced ligand is confirmed by the observation of the ammonium band at 2538 cm^{-1} , with the source of proton from the ionization of dissolved CO₂. The protonation in TAPP ligand instead of Fe center avoids the formation of Fe-H structure for further proton reduction, instead, it provides a potential proton-relay site neighboring to the reaction center. The CO₂ reduction is initiated when [Fe $^{\text{II}}$ TAPP] 0 is two electron-reduced, a trapped CO on the catalyst [Fe $^{\text{II}}$ (CO)(TAPP)] 0 is formed, followed by an instant one-electron reduction, and the steady-state species observed in IR spectra is in the form of [Fe $^{\text{II}}$ (CO)(TAPP $^-$ H $^+$)] 0 . In spectral kinetics studies for CO generation, an uncommon inverse KIE (0.59) was obtained, it indicates that the RDS for CO generation is the conversion of CO₂ to *COOH via a more efficient PCET pathway. The inner-sphere proton transfer from the protonated ligand would be the key to achieve such PCET procedure.

The CO is tightly bound to FeTAPP catalyst and impedes its cycling



Scheme 1. Proposed reaction pathways of CO₂ reduction initiated from [Fe $^{\text{II}}$ TAPP] 0 . * indicates the intermediates that was not observed in in-situ FT-IR.

for catalytic CO₂ reduction. The CO desorption occurs at a more negative potential below –1.2 V when the real catalytic reactions initiates. At this potential, another reaction pathway exists that a part of the trapped CO can be converted to CH₄ via the intermediate of *CHO. For the step, since the protonation of TAPP is observed during the whole reduction procedure, it is believed that the protonated ligand still plays the role as proton-relay to facilitate the formation of *CHO.

4. Conclusions

We have developed an operando FT-IR methodology which succeeds in the monitoring the electrochemical process of redox-noninnocent ligand catalyst in aqueous media, the synchronization between the IR data collection and electrochemical scan enables the acquirement of accurate spectral kinetics. The detailed pathway of CO₂ reduction on the state-of-art molecular catalyst of FeTAPP, especially the procedure of protonation and intramolecular proton transfer, has been revealed. By protonation on the pyrrole N during the reduction of the catalyst, the reduction of proton remarkably depressed, and the intramolecular proton transfer from the protonated pyrrole N facilitate the PCET process of CO₂ reduction to *COOH, which is experimentally demonstrated as the RDS of the CO₂ reduction to CO. This work deepens the understanding on how noninnocent ligands affects the selectivity and efficiency of CO₂ reduction and should benefit the design of the catalyst of high CO₂ reduction selectivity in aqueous media.

CRediT authorship contribution statement

Yangfan Li: Conceptualization, Methodology, Software, Investigation, Data curation, Writing – original draft. **Shijie Xie:** Methodology, Investigation, Data curation, Visualization. **Xingmiao Huang:** Methodology, Validation, Data curation. **Wenjing Song:** Writing – review & editing, Supervision. **Chuncheng Chen:** Writing – review & editing, Supervision. **Hua Sheng:** Conceptualization, Methodology, Writing – review & editing, Project administration, Funding acquisition. **Jincai Zhao:** Writing – review & editing, Supervision.

Declaration of Competing Interest

The authors declare that they have no known competing financial interests or personal relationships that could have appeared to influence the work reported in this paper.

Data Availability

Data will be made available on request.

Acknowledgements

This work was supported by the National Key Research and Development Program of China (No. 2020YFA0710303 and 2020YFC1808401), the National Natural Science Foundation of China (No. 22076193), the CAS Project for Young Scientists in Basic Research (No. YSBR-004) and the “Strategic Priority Research Program B” of the Chinese Academy of Sciences (Grant No. XDB36000000). We thank Prof. Heinz Frei, UC Berkeley, for insightful discussions.

Appendix A. Supporting information

Supplementary data associated with this article can be found in the online version at [doi:10.1016/j.apcatb.2023.122542](https://doi.org/10.1016/j.apcatb.2023.122542).

References

- [1] N. Kinzel, C.W. Werle, W. Leitner, Transition metal complexes as catalysts for the electroconversion of CO₂: an organometallic perspective, *Angew. Chem. Int. Ed.* 60 (2021) 11628–11686.
- [2] P. Kang, Z. Chen, A. Nayak, S. Zhang, T.J. Meyer, Single catalyst electrocatalytic reduction of CO₂ in water to H₂+CO syngas mixtures with water oxidation to O₂, *Energy Environ. Sci.* 7 (2014) 4007–4012.
- [3] A.N. Marianov, Y. Jiang, Covalent ligation of Co molecular catalyst to carbon cloth for efficient electroreduction of CO₂ in water, *Appl. Catal. B Environ.* 244 (2019) 881–888.
- [4] W.J. Zhang, Y. Hu, L.B. Ma, G.Y. Zhu, Y.R. Wang, X.L. Xue, R.P. Chen, S.Y. Yang, Z. Jin, Progress and perspective of electrocatalytic CO₂ reduction for renewable carbonaceous fuels and chemicals, *Adv. Sci.* 5 (2018), 1700275.
- [5] Y.Y. Birdja, E. Pérez-Gallent, M.C. Figueiredo, A.J. Göttle, F. Calle-Vallejo, M.T. M. Koper, Advances and challenges in understanding the electrocatalytic conversion of carbon dioxide to fuels, *Nat. Energy* 4 (2019) 732–745.
- [6] I. Sievert, Proton-coupled electron transfer reactions catalysed by 3 d metal complexes, *Chem. Eur. J.* 21 (2015) 15078–15091.
- [7] D.G. Nocera, Proton-coupled electron transfer: the engine of energy conversion and storage, *J. Am. Chem. Soc.* 144 (2022) 1069–1081.
- [8] S. Gong, W. Wang, R. Lu, M. Zhu, H. Wang, Y. Zhang, J. Xie, C. Wu, J. Liu, M. Li, S. Shao, G. Zhu, X. Lv, Mediating heterogenized nickel phthalocyanine into isolated Ni-N₂ moiety for improving activity and stability of electrocatalytic CO₂ reduction, *Appl. Catal. B Environ.* 318 (2022), 121813.
- [9] S. Gu, A.N. Marianov, Y. Jiang, Covalent grafting of cobalt aminoporphyrin-based electrocatalyst onto carbon nanotubes for excellent activity in CO₂ reduction, *Appl. Catal. B Environ.* 300 (2022), 120750.
- [10] D.-D. Ma, S.-G. Han, C. Cao, X. Li, X.-T. Wu, Q.-L. Zhu, Remarkable electrocatalytic CO₂ reduction with ultrahigh CO/H₂ ratio over single-molecularly immobilized pyrrolidinonyl nickel phthalocyanine, *Appl. Catal. B Environ.* 264 (2020), 118530.
- [11] C. Römel, J. Song, M. Tarrago, J.A. Rees, M. van Gastel, T. Weyhermüller, S. DeBeer, E. Bill, F. Neese, S. Ye, Electronic structure of a formal iron(0) porphyrin complex relevant to CO₂ reduction, *Inorg. Chem.* 56 (2017) 4745–4750.
- [12] David L. Hickman, Atoollah Shirazi, H.M. Goff, Deuterium NMR spectroscopic studies of low-valent iron porphyrin species, *Inorg. Chem.* 24 (1985) 563–566.
- [13] X.F. Lu, H.A. Ahsaine, B. Dereli, A.T. García-Espaza, M. Reinhard, T. Shinagawa, D.X. Li, K. Adil, M.R. Tchala, T. Kroll, M. Eddaoudi, D. Sokaras, L. Cavallo, K. Takanebe, Operando elucidation on the working state of immobilized fluorinated iron porphyrin for selective aqueous electroreduction of CO₂ to CO, *ACS Catal.* 11 (2021) 6499–6509.
- [14] B. Mondal, S. Ye, Hidden ligand noninnocence: a combined spectroscopic and computational perspective, *Coord. Chem. Rev.* 405 (2020), 213115.
- [15] Y.-Q. Zhang, J.-Y. Chen, P.E.M. Siegbahn, R.-Z. Liao, Harnessing noninnocent porphyrin ligand to circumvent Fe-hydride formation in the selective Fe-Catalyzed CO₂ reduction in aqueous solution, *ACS Catal.* 10 (2020) 6332–6345.
- [16] A.J. Göttle, M.T.M. Koper, Determinant role of electrogenerated reactive nucleophilic species on selectivity during reduction of CO₂ catalyzed by metalloporphyrins, *J. Am. Chem. Soc.* 140 (2018) 4826–4834.
- [17] H. Sheng, H. Frei, Direct observation by rapid-scan FT-IR spectroscopy of two-electron-reduced intermediate of tetraazza catalyst [Co^{II}N₄H(MeCN)]²⁺ Converting CO₂ to CO, *J. Am. Chem. Soc.* 138 (2016) 9959–9967.
- [18] H. Sheng, M.H. Oh, W.T. Osowiecki, W. Kim, A.P. Alivisatos, H. Frei, Carbon dioxide dimer radical anion as surface intermediate of photoinduced CO₂ reduction at aqueous Cu and CdSe nanoparticle catalysts by rapid-scan FT-IR spectroscopy, *J. Am. Chem. Soc.* 140 (2018) 4363–4371.
- [19] W. Wang, C. Deng, S. Xie, Y. Li, W. Zhang, H. Sheng, C. Chen, J. Zhao, Photocatalytic C-C coupling from carbon dioxide reduction on copper oxide with mixed-valence copper(I)/Copper(II), *J. Am. Chem. Soc.* 143 (2021) 2984–2993.
- [20] H. Zhang, Y. Li, J. Wang, N. Wu, H. Sheng, C. Chen, J. Zhao, An unprecedent hydride transfer pathway for selective photocatalytic reduction of CO₂ to formic acid on TiO₂, *Appl. Catal. B Environ.* 284 (2021), 119692.
- [21] H. Rao, L.C. Schmidt, J. Bonin, M. Robert, Visible-light-driven methane formation from CO₂ with a molecular iron catalyst, *Nature* 548 (2017) 74–77.
- [22] C. Costentin, M. Robert, J.M. Savéant, A. Tatin, Efficient and selective molecular catalyst for the CO₂-to-CO electrochemical conversion in water, *Proc. Natl. Acad. Sci. U. S. A.* 112 (2015) 6882–6886.
- [23] X. Li, S. Wang, L. Li, Y. Sun, Y. Xie, Progress and perspective for in situ studies of CO₂ reduction, *J. Am. Chem. Soc.* 142 (2020) 9567–9581.
- [24] Zhi-You Jun-Tao Li, Ian Zhou, S.-G. Broadwell Sun, In-Situ Infrared Spectroscopic Studies of Electrochemical Energy Conversion and Storage, *Acc. Chem. Res.* 45 (2012) 485–494.
- [25] R. Kas, O. Ayemoba, N.J. Firet, J. Middelkoop, W.A. Smith, A. Cuesta, In-situ infrared spectroscopy applied to the study of the electrocatalytic reduction of CO₂: theory, practice and challenges, *ChemPhysChem* 20 (2019) 2904–2925.
- [26] S. Zhu, T. Li, W.-B. Cai, M. Shao, CO₂ electrochemical reduction as probed through infrared spectroscopy, *ACS Energy Lett.* 4 (2019) 682–689.
- [27] S. Nitopi, E. Bertheussen, S.B. Scott, X. Liu, A.K. Engstfeld, S. Horch, B. Seger, I.E. L. Stephens, K. Chan, C. Hahn, J.K. Nørskov, T.F. Jaramillo, I. Chorkendorff, Progress and perspectives of electrochemical CO₂ reduction on copper in aqueous electrolyte, *Chem. Rev.* 119 (2019) 7610–7672.
- [28] R. Francke, B. Schille, M. Roemelt, Homogeneously catalyzed electroreduction of carbon dioxide-methods, mechanisms, and catalysts, *Chem. Rev.* 118 (2018) 4631–4701.

- [29] C.W. Machan, M.D. Sampson, S.A. Chabolla, T. Dang, C.P. Kubiak, Developing a mechanistic understanding of molecular electrocatalysts for CO₂ reduction using infrared spectroelectrochemistry, *Organometallics* 33 (2014) 4550–4559.
- [30] O. Brummel, F. Waidhas, U. Bauer, Y. Wu, S. Bochmann, H.P. Steinruck, C. Papp, J. Bachmann, J. Libuda, Photochemical energy storage and electrochemically triggered energy release in the norbornadiene-quadracyclane system: UV photochemistry and IR spectroelectrochemistry in a combined experiment, *J. Phys. Chem. Lett.* 8 (2017) 2819–2825.
- [31] C. Costentin, M. Robert, J.M. Savéant, Current issues in molecular catalysis illustrated by iron porphyrins as catalysts of the CO₂-to-CO electrochemical conversion, *Acc. Chem. Res.* 48 (2015) 2996–3006.
- [32] Y.-H. Zhang, W.-J. Ruan, Z.-Y. Li, Y. Wu, J.-Y. Zheng, DFT study on the influence of meso-phenyl substitution on the geometric, electronic structure and vibrational spectra of free base porphyrin, *Chem. Phys.* 315 (2005) 201–213.
- [33] M. Aydin, DFT and Raman spectroscopy of porphyrin derivatives: tetraphenylporphine (TPP), *Vib. Spectrosc.* 68 (2013) 141–152.
- [34] Z.C. Sun, Y.B. She, Y. Zhou, X.F. Song, K. Li, Synthesis, characterization and spectral properties of substituted tetraphenylporphyrin iron chloride complexes, *Molecules* 16 (2011) 2960–2970.
- [35] Ying-Hui Zhang, Dong-Ming Chen, Tianjing He, F.-C. Liu, Raman and infrared spectral study of meso-sulfonatophenyl substituted porphyrins (TPPS_n, n=1, 2A, 2O, 3, 4), *Spectrochim. Acta A* 59 (2003) 87–101.
- [36] W. Kaim, Manifestations of noninnocent ligand behavior, *Inorg. Chem.* 50 (2011) 9752–9765.
- [37] C. Dong, X. Song, E.J. Meijer, G. Chen, Y. Xu, J. Yu, Mechanism studies on thermal dissociation of tri-n-octylamine hydrochloride with FTIR, TG, DSC and quantum chemical methods, *J. Chem. Sci.* 129 (2017) 1431–1440.
- [38] Abel Locati, Michel Berthelot, Michel Evain, Jacques Lebreton, Jean-Yves Le Questel, Monique Mathé-Allainmat, Aurélien Planchat, Eric Renault, J. Graton, The exceptional hydrogen-bond properties of neutral and protonated lobeline, *J. Phys. Chem. A* 111 (2007) 6397–6405.
- [39] K.M. Harmon, S. Pillar, Hydrogen bonding. Part 84. Infrared spectral evidence for three-center NHF bonds in a variety of tertiary amine-hydrogen fluoride compounds, *J. Mol. Struct.* 740 (2005) 75–80.
- [40] Y. Liu, Z. Zhang, H. Wang, Y. Wang, Toward efficient single-atom catalysts for renewable fuels and chemicals production from biomass and CO₂, *Appl. Catal. B Environ.* 292 (2021), 120162.
- [41] J.-M. Savéant, Molecular catalysis of electrochemical reactions. mechanistic aspects, *Chem. Rev.* (2008) 2348–2378.
- [42] C. Costentin, S. Drouet, G. Passard, M. Robert, J.M. Savéant, Proton-coupled electron transfer cleavage of heavy-atom bonds in electrocatalytic processes. Cleavage of a C-O bond in the catalyzed electrochemical reduction of CO₂, *J. Am. Chem. Soc.* 135 (2013) 9023–9031.
- [43] Y. Lin, C. Deng, L. Wu, Y. Zhang, C. Chen, W. Ma, J. Zhao, Quantitative isotope measurements in heterogeneous photocatalysis and electrocatalysis, *Energy Environ. Sci.* 13 (2020) 2602–2617.
- [44] W. Chang, C. Sun, X. Pang, H. Sheng, Y. Li, H. Ji, W. Song, C. Chen, W. Ma, J. Zhao, Inverse kinetic solvent isotope effect in TiO₂ photocatalytic dehalogenation of non-adsorbable aromatic halides: a proton-induced pathway, *Angew. Chem. Int. Ed.* 54 (2015) 2052–2056.
- [45] Y. Kim, S. Park, S.-J. Shin, W. Choi, B.K. Min, H. Kim, W. Kim, Y.J. Hwang, Time-resolved observation of C-C coupling intermediates on Cu electrodes for selective electrochemical CO₂ reduction, *Energy Environ. Sci.* 13 (2020) 4301–4311.
- [46] L. Xue, C. Zhang, J. Wu, Q.-Y. Fan, Y. Liu, Y. Wu, J. Li, H. Zhang, F. Liu, S. Zeng, Unveiling the reaction pathway on Cu/CeO₂ catalyst for electrocatalytic CO₂ reduction to CH₄, *Appl. Catal. B Environ.* 304 (2022), 120951.
- [47] H.-L. Zhu, J.-R. Huang, X.-W. Zhang, C. Wang, N.-Y. Huang, P.-Q. Liao, X.-M. Chen, Highly efficient electroconversion of CO₂ into CH₄ by a metal-organic framework with trigonal pyramidal Cu(I)N₃ active sites, *ACS Catal.* 11 (2021) 11786–11792.
- [48] X. Liu, J. Xiao, H. Peng, X. Hong, K. Chan, J.K. Nørskov, Understanding trends in electrochemical carbon dioxide reduction rates, *Nat. Commun.* 8 (2017) 15438.